processes

MDPI

Article

Process Parameter Screening Through Fractional Factorial Design for the Synthesis of Gold Nanoparticles

Harshilkumar Jani [1,2], Ketan Ranch [1,*], Vijay R. Chidrawar [3], Popat Mohite [4] and Sudarshan Singh [5,6,*]

[1] Department of Pharmaceutics, L. M. College of Pharmacy, Navrangpura, Ahmedabad 380009, India; harshil.jani@lmcp.ac.in
[2] Research Scholar, Gujarat Technological University, Chandkheda, Ahmedabad 382424, India
[3] School of Pharmacy and Technology Management, SVKM's Narsee Monjee Institute of Management Studies (NMIMS), Deemed-To-University, Green Industrial Park, TSIIC, Jadcherla, Hyderabad 509301, India; vijay.chidrawar@gmail.com
[4] AETs St. John Institute of Pharmacy and Research, Palghar 401404, India; mohitepb@gmail.com
[5] Office of Research Administration, Chiang Mai University, Chiang Mai 50200, Thailand
[6] Faculty of Pharmacy, Chiang Mai University, Chiang Mai 50200, Thailand
* Correspondence: ketan.ranch@lmcp.ac.in (K.R.); sudarshan.s@cmu.ac.th (S.S.)

Abstract

Nanoparticles (NPs) of noble metals such as gold have garnered significant attention due to their novel optical and catalytic properties, their theranostic properties, as they are biocompatible, and they attract considerable interest in a range of applications including targeted drug delivery. In this study, a fractional factorial design (FFD) is applied to systematically investigate the influence of key synthesis parameters (independent variables) at a low level (−1) and a high level (+1), including the reducing agent type (chitosan or trisodium citrate), concentration of reducing agent (10 to 40 mg), pH (3.5 to 8.5), temperature (60 to 100 °C), agitation time (5 to 15 min), and agitation speed (400 to 1200 rpm), on the dependent parameters—particle size and polydispersity index of gold nanoparticles (GNPs). The goal of this study was to provide a comprehensive understanding of the interplay between these parameters and their interaction effect on the characteristics of gold nanoparticles. A fractional factorial design allowed for efficient screening of the parameter space while minimizing the number of experiments required. The results demonstrated that pH, reducing agent, reducing agent–concentration, reducing agent–concentration of reducing agent–pH, and reducing agent–temperature interactions played significant roles in determining the particle size of the synthesized GNPs. Moreover, pH and reducing agent–concentration were identified as the major factors influencing the dispersity of the NPs. This study sheds light on the complex relationships between synthesis parameters and NP characteristics, offering an insight into the capacity for optimizing the synthesis process in order to tailor the desired properties of GNPs. The findings contribute to the growing field of NP synthesis and advance the understanding of the underlying mechanisms governing the formation of GNPs with specific size and dispersity characteristics.

Keywords: gold nanoparticles; fractional factorial design; screening; synthesis parameters; biosafety

check for updates

Academic Editor: Keith J. Stine

Received: 10 September 2025
Revised: 23 September 2025
Accepted: 30 September 2025
Published: 2 October 2025

Citation: Jani, H.; Ranch, K.; Chidrawar, V.R.; Mohite, P.; Singh, S. Process Parameter Screening Through Fractional Factorial Design for the Synthesis of Gold Nanoparticles. *Processes* **2025**, *13*, 3157. https://doi.org/10.3390/pr13103157

Copyright: © 2025 by the authors. Licensee MDPI, Basel, Switzerland. This article is an open access article distributed under the terms and conditions of the Creative Commons Attribution (CC BY) license (https://creativecommons.org/licenses/by/4.0/).

1. Introduction

Gold nanoparticles (GNPs) have a long and fascinating history that predates the scientific understanding of nanotechnology. Their unique optical properties have been exploited for

centuries, often unknowingly, in art and craftsmanship. One of the earliest examples is the Lycurgus Cup from 4th-century AD Rome, which exhibits dichroic properties, appearing green in reflected light and deep red in transmitted light due to gold and silver NPs embedded in its glass matrix [1]. Similarly, during the medieval period, colloidal gold was used to produce the vibrant red and purple hues of stained-glass windows in European cathedrals. These ancient artisans, while unaware of the nanoscale phenomena at play, empirically utilized gold's ability to generate size-dependent colors [2]. The first scientific account of colloidal gold came in the 17th century, when Andreas Cassius described the preparation of "Purple of Cassius," a gold–tin chloride complex that produced a deep purple coloration in ceramics and glass. A major milestone was achieved by Michael Faraday in 1857, who prepared stable colloidal gold solutions and recognized that their ruby-red color differed fundamentally from bulk gold. Faraday attributed this to the small size of gold particles and their interaction with light phenomena now understood as localized surface plasmon resonance (LSPR) [3]. With the advent of electron microscopy in the mid-20th century, scientists were able to directly observe GNPs, paving the way for their application in biology. Immunogold labeling, where GNPs conjugated to antibodies are used as markers in electron microscopy, became a key technique for visualizing cellular structures. In recent decades, the development of nanotechnology has transformed GNPs into versatile tools across disciplines. Their biocompatibility, tunable size and shape, and ease of surface functionalization have led to applications in drug delivery [4,5], diagnostics [6], photothermal therapy [7], catalysis [8], environmental sensing [9], and advanced materials [10]. GNPs continue to play a central role in nanomedicine and materials science, making them one of the most important and well-studied nanomaterials in contemporary research.

GNPs used for drug delivery are synthesized through various methods employing different chemical reagents, with the chemical reduction method being the most versatile and widely used. Synthesis of GNPs via the chemical reduction method follows the simple Turkevich method [11,12] in the aqueous phase and proceeds to the complex Brust–Schiffrin method [13] and Oleylamine method [14] in the organic phase. The reagents used in the modified methods often use a variety of chemicals. Sodium borohydride causes reproductive or developmental harm [15], cetyltrimethylammonium bromide (CTAB) is highly toxic to cells at sub-micromolar concentrations, toxic to aquatic life, and may cause organ damage through repeated exposure [16], while oleylamine may cause damage to the liver, gastrointestinal tract, and immune system [17].

Hence, the safer green synthesis methods are gaining attention as they offer safer, cheaper, and as environmentally sustainable alternatives. Chitosan [CS] is a natural polysaccharide and is widely used in the pharmaceutical industries, as well as the food industries, due to its high biocompatibility and biodegradability with low toxicity [18,19]. Commercially, the bioactive polymer CS is synthesized through the deacetylation process of chitin, which is collected from the outer skeleton of crab, shrimp, lobster, and crayfish shells [20]. Structurally, CS is a cationic biopolymer consisting of D-glucosamine and N-acetyl D-glucosamine units attached by β-1,4 glycosidic bonds. Biopolymer CS has two types of bioactive functional groups, the hydroxyl group and the amino group, and these active groups are responsible for the potential antimicrobial activity of CS [20,21]. CS is a positively charged molecule due to the presence of $–NH3^{+}$ groups, and these active amino groups are also responsible for the interaction with the negatively charged cell membranes of bacteria [21,22]. While CS is commonly used in drug delivery applications, it is also used as a stabilizing agent for the synthesis of different metallic nanoparticles. It can facilitate the modification of the surface physical absorption and electrostatic interaction, thus improve the stability and bioactivity of nanoparticles and making them perfect candidates as potential therapeutic agents [23–26]. Meanwhile, reduction using trisodium citrate is

versatile and a safer option in the preparation of negatively charged GNPs. CS and TSC serve a dual purpose, in that they reduce Au^{+3} to Au^{0} and stabilize the GNPs by imparting strong positive and negative surface charges. Despite the understanding gained to date of the reducing and stabilizing mechanism, the process parameters significantly affect the synthesis of GNPs, which needs to be studied.

In this study, the process parameters for the synthesis of CS-functionalized gold nanoparticles was investigated through a fractional factorial design. A 2^{6-2} fractional factorial design was utilized to screen process parameters affecting the size and polydispersity of the GNPs. Two different types of GNPs were prepared based on the surface charge and applicability. Positively charged gold nanoparticles were prepared using chitosan as the reducing agent, while trisodium citrate was used to prepare negatively charged GNPs. This study aimed to explore the roles of the reducing agent, concentration of reducing agent, pH, reducing temperature, agitation speed, and agitation time in the synthesis of positively charged and negatively charged GNPs.

2. Materials and Methods

2.1. Materials

Chitosan (low MW) extra pure, 10–150 m·Pas, 90% DA; gold chloride trihydrate (tetrachloroauric acid ($HAuCl_4$)); and sodium citrate tribasic dihydrate extra pure, 98% were procured from Sisco Research Laboratories Pvt. Ltd., Mumbai, Maharashtra, India. Glacial acetic acid, nitric acid, and hydrochloric acid were procured from Actylis, Vasna Chacharavadi, Gujarat, India. Ultrapurified water was produced from a Milli-Q water assembly (DirectQ-8, Merck, Cambridge, MA, USA) with a resistivity of 18.2 MΩ·cm. Ultrapurified water was utilized in the preparation of all reactions. All other chemicals and reagents were used at analytical grade. All chemicals were procured from reputed suppliers and used without any further purification.

2.2. Software and Instrumentation

Design Expert® 13.0.1 (Trial Version, Stat-Ease, Minneapolis, MN, USA) was used for plotting the fractional factorial design. A UV Spectrophotometer-1900 (Shimadzu, Tokyo, Japan) was used for a surface plasmon resonance effect, and a Malvern Zetasizer Nano ZS (Malvern Panalytical Ltd., Malvern, UK) was used for the hydrodynamic particle size, polydispersity index, and zeta potential. A Milli-Q assembly was used to produce ultrapure water.

2.3. Fractional Factorial Experimental Design

Fractional factorial designs are one the most widely used for screening purposes, as they enable the evaluation of a large number of input factors with a reduced number of experiments required [27,28]. The fractional factorial design (FFD) was employed to systematically screen and identify the significant process parameters affecting the synthesis of CS-functionalized GNPs. A 2^{k-p} fractional factorial design was chosen, where k represents the number of factors studied and p denotes the fraction of the full factorial matrix. A 2^{6-2} fractional factorial design was employed to identify the critical process parameters influencing the synthesis of GNPs. This statistical design enables the efficient evaluation of the main effects and selected interaction effects of multiple factors using a reduced number of experimental runs, compared to a full factorial design. In this study, six independent variables—(X1) type of reducing agent, (X2) concentration of reducing agent, (X3) reaction temperature, (X4) pH of the reaction medium, (X5) stirring speed, and (X6) stirring time—were screened at two levels (high and low). The main effect of these factors was studied on one important formulation attribute, i.e., particle size (PS) or polydispersity index (PDI). A 2^{6-2} design (one-quarter fraction) was selected, resulting in 16 experimental

runs. The experimental matrix was generated using Design Expert® Software (Trial Version 13, Stat-Ease Inc., Minneapolis, MN, USA), and the runs were randomized to minimize systematic errors. Randomization may increase setup costs and experimental complexity, but it is indispensable for ensuring that observed effects truly represent the underlying processes being studied rather than experimental artifacts, thereby maintaining the integrity and reliability of the fractional factorial screening experiment [29]. Independent and dependent variables for the fractional factorial design are shown in Table 1. Table 2 shows the fractional factorial design matrix with coded values, where X1 is a categorical factor and the rest are numeric factors.

Table 1. Independent and dependent variables for fractional factorial design.

Independent Variable		
Factor	**High Level (+1)**	**Low Level (−1)**
Type of reducing agent (X1)	Trisodium citrate	Chitosan (low molecular weight)
Concentration of reducing agent (X2)	40 mg	10 mg
Temperature (X3)	100 °C	60 °C
pH (X4)	8.5	3.5
Stirring speed (X5)	1200 rpm	400 rpm
Stirring time (X6)	15 min	5 min
Dependent Variable		
Particle size (Y1)	nm	
Polydispersity index (Y2)	Unitless	

Table 2. Fractional factorial design matrix with coded values.

	X1	**X2**	**X3**	**X4**	**X5**	**X6**
Batch	**A: Type of Reducing Agent**	**B: Concentration of Reducing Agent**	**C: Temperature**	**D: pH**	**E: Stirring Speed**	**F: Stirring Time**
		mg	**°C**		**rpm**	
1	−1	−1	−1	−1	−1	−1
2	1	−1	−1	−1	1	−1
3	−1	1	−1	−1	1	1
4	1	1	−1	−1	−1	1
5	−1	−1	1	−1	1	1
6	1	−1	1	−1	−1	1
7	−1	1	1	−1	−1	−1
8	1	1	1	−1	1	−1
9	−1	−1	−1	1	−1	1
10	1	−1	−1	1	1	1
11	−1	1	−1	1	1	−1
12	1	1	−1	1	−1	−1
13	−1	−1	1	1	1	−1
14	1	−1	1	1	−1	−1
15	−1	1	1	1	−1	1
16	1	1	1	1	1	1

2.4. Preparation of Citrate-Capped (Cit-GNP) and Chitosan-Capped (CS-GNP) Gold Nanoparticles

All glassware used for this study was washed with freshly prepared Aqua Regia solution (HNO_3:HCl:: 1:3). For the preparation of GNPs, chemical reduction of $HAuCl_4$ was used in both methods. *Citrate-capped GNPs*: The modified Turkevich method was employed as reported [12]; in brief, 20 mL of ultrapurified water was poured into a 50 mL conical flask, and 1 mL of 10 mM $HAuCl_4$ solution was added. The pH of the solution was adjusted using 0.1% HCl or 0.1% NaOH. The flask was heated to 90 °C using a hot plate with a magnetic stirrer (REMI 2MLH, Mumbai, India). The conical flask was kept closed to keep the reaction volume constant. This reaction mixture was kept at 800 rpm. To this, 1 mL of 1% trisodium citrate solution was added dropwise to ensure the maximum homogeneity. The reaction mixture turned from pale yellow to a red wine color; this was an indication of the synthesis of GNPs. The prepared mixture was further stirred for 15 min and cooled down to room temperature. The prepared GNPs were stored in the refrigerator at 4 °C for further use. *Chitosan-capped GNPs*: CS solution was prepared using low-molecular-weight CS. We prepared 0.2% CS solution in 1% glacial acetic acid, and 20 mL of CS solution was taken. The pH of the solution was adjusted using 0.1% HCl or 0.1% NaOH. This CS solution was heated using a hot plate with a magnetic stirrer (REMI 2MLH, Mumbai, India) to 90 °C. The volume was kept constant, and conical flasks were covered with aluminum foil. We added 1 mL of 10 mM solution of chloric acid rapidly to this solution, and the reaction mixture turned a dark blue color and eventually a wine red color; this indicated the synthesis of GNPs. The dispersion was stored at 4 °C in a refrigerator for further use. Figure 1 shows the schematic diagrams of citrate-capped GNPs (A) and CS-capped GNPs (B).

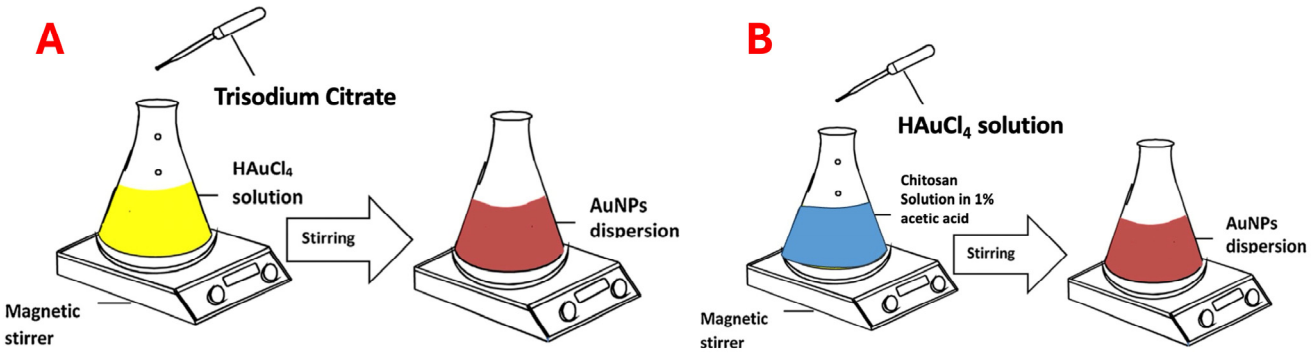


Figure 1. Synthesis method for (**A**) citrate-capped and (**B**) CS-capped gold nanoparticles.

2.5. Local Surface Plasmon Resonance Effect

The LSPR effect of GNPs was evaluated using a UV-Vis spectrophotometer (UV−1900, Shimadzu, Tokyo, Japan). The GNP suspension was diluted 10-fold using ultrapure water to minimize scattering effects and bring the absorbance within the optimal measurement range of the instrument. The diluted GNP sample was placed in a clean quartz cuvette (1 cm path length), and the absorbance spectrum was recorded from 800 to 200 nm using a UV spectrophotometer (UV−1900, Shimadzu, Tokyo, Japan) with baseline correction against ultrapure water, to analyze the LSPR peak position and shape.

2.6. Particle Size, Zeta Potential, and Polydispersity Index

The hydrodynamic particle size, PDI, and zeta potential [30] of the Cit-GNPs and CS-GNPs were determined using a Malvern Zetasizer Nano ZS (Malvern Panalytical Ltd., Malvern, UK) based on dynamic light scattering (DLS) and electrophoretic light scattering (ELS) principles as reported [31] The GNP suspension was diluted 10-fold with ultrapure water to avoid multiple scattering effects and ensure the optimal sample concentration. Measurements were performed at 25 °C in a disposable polystyrene cuvette (for size and

PDI) and in a folded capillary cell (for ZP). During the analysis, the GNP concentration was maintained, and the instrument's count rate (kcps) was maintained above 350 kcps to achieve better accuracy and reliable results. Each measurement was carried out in triplicate, and the results were expressed as the mean ± standard deviation.

2.7. Transmission Electron Microscopy

The morphology of Cit-GNPs and CS-GNPs was observed using high-resolution transmission electron microscopy (FEI, Tecnai G2, F30, Thermo Fisher Scientific, Waltham, MA, USA) [32]. Both dispersions were diluted 10 times with ultrapurified water, and drops of Cit-GNP and CS-GNP dispersions were placed on a carbon-coated copper grid stained with a 0.5% aqueous solution of phosphotungstic acid. This was directly positioned, then air-dried, prior to being imaged using a 300 keV acceleration voltage. Using different combinations of bright-field imaging at an increasing magnification up to 40,000×, the morphology and size of the GNPs were observed.

2.8. Fourier-Transform Infrared Spectroscopy

The Fourier-transform infrared (FTIR) spectra of the samples were recorded to confirm the presence of chitosan on the surfaces of CS-GNPs. The analysis was performed using a Fourier-transform infrared spectrophotometer (IRSpirit, Shimadzu, Tokyo, Japan) in the range of 4000–400 cm^{-1}. Samples were directly placed on the ATR crystal, and spectra were recorded at a resolution of 4 cm^{-1} with 32 scans per sample.

2.9. Gold Quantification by Inductively Coupled Plasma–Optical Emission Spectrometer

Gold quantification was performed using an inductively coupled plasma–optical emission spectrometer (Avio 200 ICP-OES, Perkin Elmer, Hopkinton, MA, USA). The ICP-OES system employed a simultaneous optical emission detection system with high-resolution capabilities suitable for trace metal analysis. Both the samples were digested in aqua regia ($HCl:HNO_3$, 3:1 v/v), diluted with ultrapure water, and analyzed against a calibration curve prepared from gold standards (LOD: 0.031 µg/mL, $R^2 > 0.999$). Optimized instrumental parameters are presented in Table 3.

Table 3. Optimized ICP-OES instrumental parameters.

Parameter	Value
RF Power	1200 W
Plasma Gas Flow	15 L/min
Auxiliary Gas Flow	0.2 L/min
Nebulizer Gas Flow	0.65 L/min
Sample Uptake Rate	1.5 mL/min
Integration Time	10 s
Wavelength	242.7 nm (Primary), 267.5 nm (Secondary)

2.10. Biocompatibility of Gold Nanoparticles

The biocompatibility of Cit-GNPs and CS-GNPs was tested against HaCaT and CaCO-2 cells as reported [31,33]. Briefly, the cells were cultured in high-glucose medium (Dulbecco's modified Eagle's medium—DMEM), supplemented with 10% fetal bovine serum and penicillin–streptomycin (pen/strep-5000 U/mL). The cells (HaCaT and CaCO-2) were separately seeded at a density of 1×10^4 cells/well in a 96-well plate and incubated at 37 °C under a 5% CO_2 (5%) atmosphere until a confluence of 80% was reached. The cells were individually treated with Cit-GNPs and CS-GNPs at varied concentrations (3.12 µg/mL

to 100 µg/mL), while the CS was tested at 100 µg/mL, and we compared the viability against untreated cells. The viability was analyzed using an MTT assay at 560 nm using a microplate reader, and the background was subtracted with the measured OD at 670 nm.

2.11. Statistical Analysis

All experiments were conducted in triplicate and repeated in two independent studies to ensure their reliability. The collected data were analyzed using analysis of variance (ANOVA), followed by Dunn's test to determine significant differences between groups. A significance threshold of $p < 0.05$ was applied throughout this study to assess statistical significance.

3. Results

3.1. Fractional Factorial Design

All the responses (dependent variables) observed for the 16 batches were simultaneously fitted to the 2FI model using Design the Expert (Stat-Ease Inc., Minneapolis, MN, USA). The observed dependent variables (Y1 and Y2) for the Cit-GNPs and CS-GNPs are shown in Table 4.

Table 4. Measured response (Y1 and Y2) of fractional factorial design.

	X1	X2	X3	X4	X5	X6	Y1	Y2
Run	**Type of Reducing Agent**	**Concentration of Reducing Agent**	**Temperature**	**pH**	**Stirring Speed**	**Stirring Time**	**Particle Size**	**PDI**
		mg	**Celsius**		**rpm**		**nm**	
1	Chitosan	10	60	3.5	400	5	325.7	0.54
2	Trisodium Citrate	10	60	3.5	1200	5	96.69	0.55
3	Chitosan	40	60	3.5	1200	15	101.4	0.28
4	Trisodium Citrate	40	60	3.5	400	15	162.7	0.176
5	Chitosan	10	100	3.5	1200	15	71.3	0.48
6	Trisodium Citrate	10	100	3.5	400	15	381.8	0.27
7	Chitosan	40	100	3.5	400	5	45.65	0.44
8	Trisodium Citrate	40	100	3.5	1200	5	446.3	0.225
9	Chitosan	10	60	8.5	400	15	598.2	0.772
10	Trisodium Citrate	10	60	8.5	1200	15	159.6	0.39
11	Chitosan	40	60	8.5	1200	5	293.7	0.49
12	Trisodium Citrate	40	60	8.5	400	5	1219	0.394
13	Chitosan	10	100	8.5	1200	5	523.2	0.704
14	Trisodium Citrate	10	100	8.5	400	5	628.4	0.97
15	Chitosan	40	100	8.5	400	15	176	0.24
16	Trisodium Citrate	40	100	8.5	1200	15	948.9	0.878

3.2. Effect of Independent Variables on Particle Size

The particle size of gold nanoparticles synthesized using CS and trisodium citrate as reducing agents showed significant variation, ranging from 45.65 nm to 1219 nm, demonstrating the profound influence of process parameters on GNPs' formation. The experimental data revealed that pH emerged as the dominant factor affecting the particle size, with a coefficient of 182.22 in the coded equation, indicating that alkaline conditions (pH 8.5) consistently produced larger particles compared to acidic conditions (pH 3.5). The type of reducing agent (CS vs. trisodium citrate) demonstrated the second most significant effect, where CS consistently produced smaller nanoparticles compared to trisodium citrate under

identical conditions. Temperature effects were moderate, with higher temperatures (100 °C vs. 60 °C) generally promoting faster reduction kinetics and slightly larger particle formation. The actual equations for Cs-GNPs and Cit-GNPs are shown in Equations (1) and (2). The ANOVA model for the particle size is shown in Table 5. Contour plots for the CS-GNPs and Cit-GNPs are shown in Figure 2.

For CS,

$$Particle\ Size(Y1) - Cs - GNP = 425.56 + 0.52X2 - 3.14X3 + 85.83X4 - 0.14X5 - 12.23X6 - 1.33X2X4 \quad (1)$$

For trisodium citrate,

$$Particle\ Size(Y1) - Cit - GNP = 105.60 - 12.40X2 + 4.79X3 - 10.69X4 - 0.14X5 - 12.23X6 + 4.16X2X4 \quad (2)$$

Table 5. ANOVA model for particle size.

Particle Size	*p*-Value
Model	0.0199
A—Type of reducing agent	0.0284
B—Concentration of reducing agent	0.3950
C—Temperature	0.7044
D—pH	0.0046
AB	0.0110
AC	0.1045
AD	0.2627
BD	0.2493
ABD	0.0475

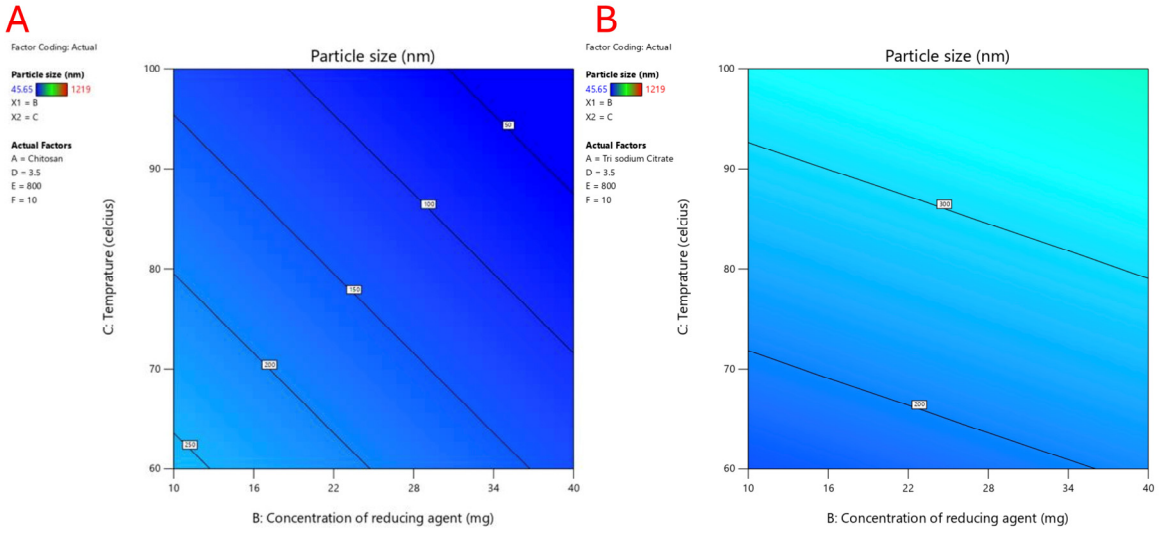


Figure 2. Contour plot of effect of CS (**A**) and trisodium citrate (**B**) on particle size, with effect of reducing agent and temperature when parameters D, E, and F are kept constant.

3.3. Effect of Independent Variables on PDI

The PDI varied significantly from 0.176 to 0.970, indicating a wide range of particle size distributions achievable through parameter optimization. pH again emerged as the most influential factor for PDI control, with a coefficient of 0.117, where lower-pH conditions (3.5) consistently produced more monodisperse populations (lower PDI values) compared to

higher-pH conditions (8.5). The three-way interaction effect between the reducing agent type, concentration, and stirring time (ABF) showed a significant effect, highlighting the complex interplay between these parameters in determining size distribution uniformity. Concentration of reducing agent effects on the PDI were notably negative (−0.097), indicating that higher concentrations of reducing agents generally led to more uniform particle populations. The interaction between the concentration of reducing agent and the stirring time (BF = 0.055) suggests that optimal stirring conditions depend on the reducing agent concentration used. Pareto charts for particle size and the PDI are shown in Figure 3. Actual equations for CS-GNPs and Cit-GNPs are shown in Equations (3) and (4). The ANOVA model for the PDI is shown in Table 6. Contour plots for the CS-GNPs and Cit-GNPs are shown in Figure 4.

For CS,

$$PDI(Y2) - Cs - GNP = 0.464 - 0.001X2 - 0.001X3 + 0.046X4 + 0.007X6 - 0.000X2X6 \quad (3)$$

For trisodium citrate,

$$PDI(Y2) - Cit - GNP = 0.535 - 0.025X2 + 0.005X3 + 0.046X4 - 0.064X6 + 0.002X2X6 \quad (4)$$

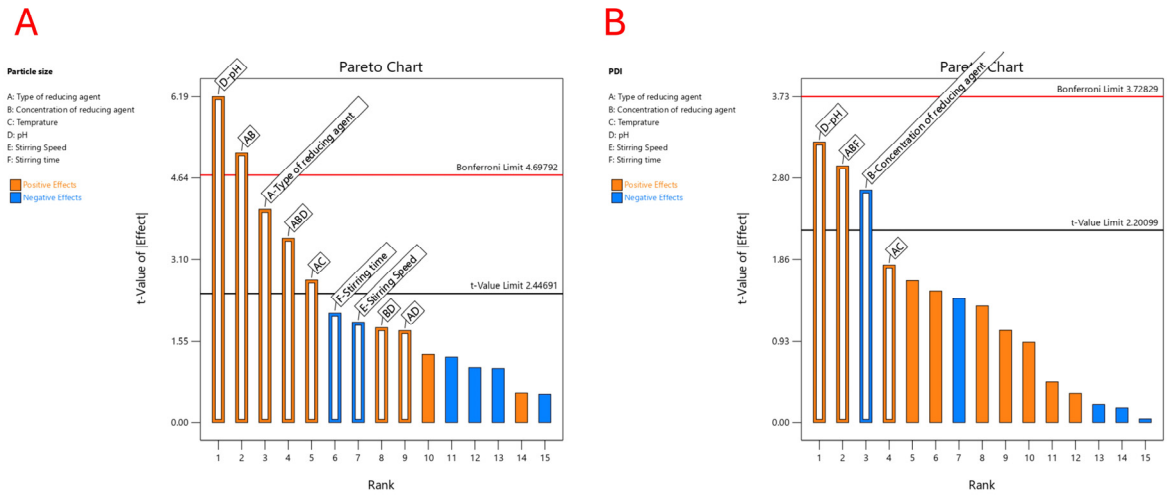


Figure 3. Pareto charts for particle size (**A**) and PDI (**B**).

Table 6. ANOVA model for PDI.

PDI	*p*-Value
Model	0.0429
A—Type of reducing agent	0.8381
B—Concentration of reducing agent	0.0220
C—Temperature	0.2230
D—pH	0.0117
F—Stirring time	0.1247
AB	0.2752
AC	0.0695
AD	0.0912
AF	0.9596
BF	0.1091
ABF	0.0159

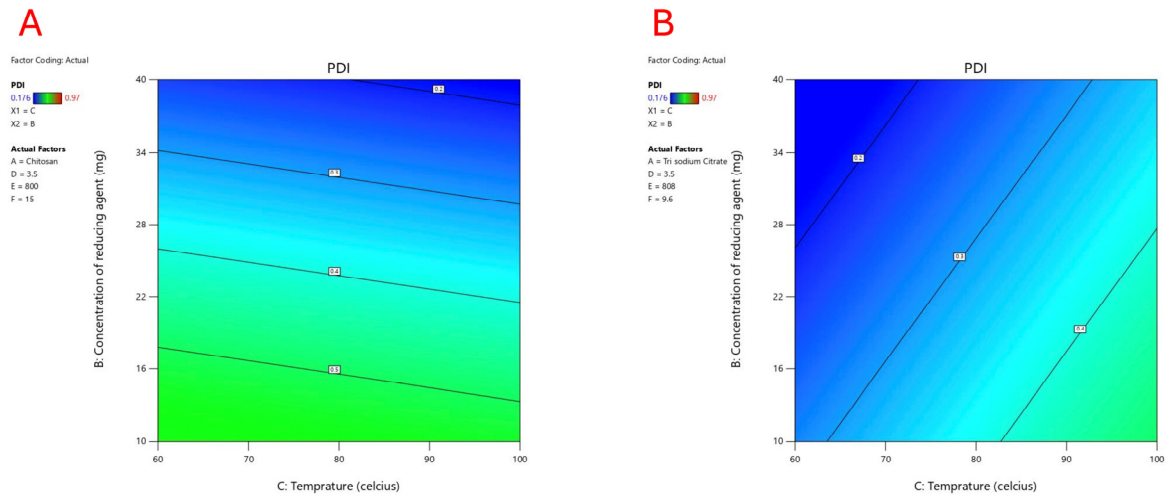


Figure 4. Contour plots of effect of CS (**A**) and trisodium citrate (**B**) on PDI, with effect of reducing agent and temperature when parameters D, E, and F are kept constant.

3.4. Preparation of Citrate-Capped (Cit-GNP) and Chitosan-Capped (CS-GNP) Gold Nanoparticles

3.4.1. Surface Plasmon Resonance Effect

GNPs exhibits a unique optical property known as surface plasmon resonance [34]. SPR arises due to the collective oscillation of conduction band electrons in response to incident light at specific wavelengths. This phenomenon results in a strong absorption band in the visible region, which is highly sensitive to the particle size, shape, aggregation state, and surrounding medium. The particle size and polydispersity play a crucial role in the SPR effect. Large particles with a high PDI show a red shift, whereas uniform particles show the SPR effect in the range of 520–525 nm [35]. The shift in SPR wavelength was confirmed with the particle size and PDI in all batches. SPR effects of all batches are shown in Figure 5.

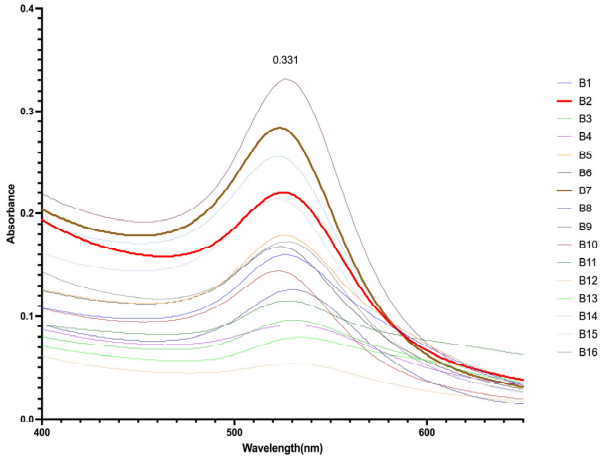


Figure 5. Local surface plasmon resonance effect of all 16 batches (10× diluted with ultrapurified water).

3.4.2. Particle Size, Zeta Potential, and PDI

The dynamic light scattering intensity plots show a bimodal nanoparticle population with an average hydrodynamic diameter of ~45.68 nm when using CS as the reducing agent, whereas the TSC yields GNPs with a hydrodynamic diameter of 96.69 nm. The electrophoretic mobility measurement gives a zeta potential; here, positively charged GNPs showed a ZP of 39.4 ± 5.8 and negatively charged GNPs showed a ZP of −31.8 ± 4.5, suggesting strong colloidal stability due to electrostatic repulsion. Particle size graphs are shown in Figure 6. Zeta potentials of both batches are shown in Figure 7.

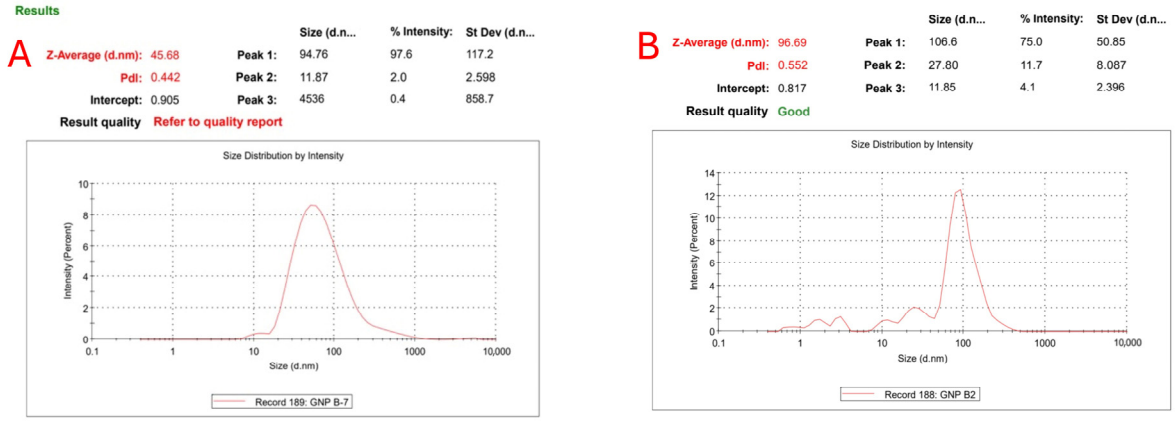


Figure 6. Hydrodynamic particle size and PDI graphs for CS-GNPs (**A**) and Cit-GNPs (**B**).

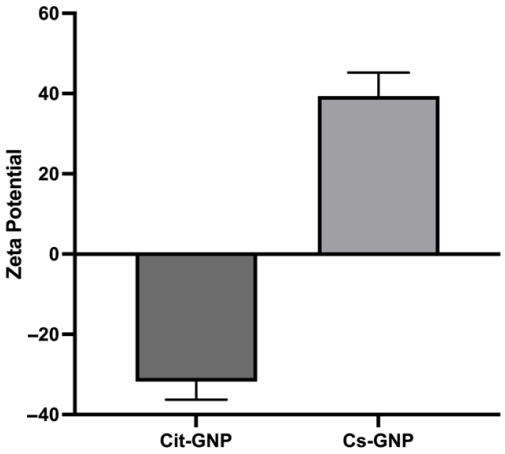


Figure 7. Zeta potential of Cit-GNPs and CS-GNPs.

3.4.3. Transmission Electron Microscopy

The TEM images of Cit-GNPs and CS-GNPs showed spherical GNPs, as can be seen in Figure 8. Both show Cit-GNPs and CS-GNPs with a spherical morphology, with no aggregation, which indicates the good stability of GNPs. TEM characterization shows a particle size of 16.36 ± 2.45 nm for Cit-GNPs, and for CS-GNPs, it shows a particle size of 18.96 ± 5.87 nm. The difference in hydrodynamic diameter arose because of the stern layer and slipping pane of both GNPs. In CS-GNPs, some were entrapped in the CS matrix, indicating the additional coating effect of chitosan on GNPs.

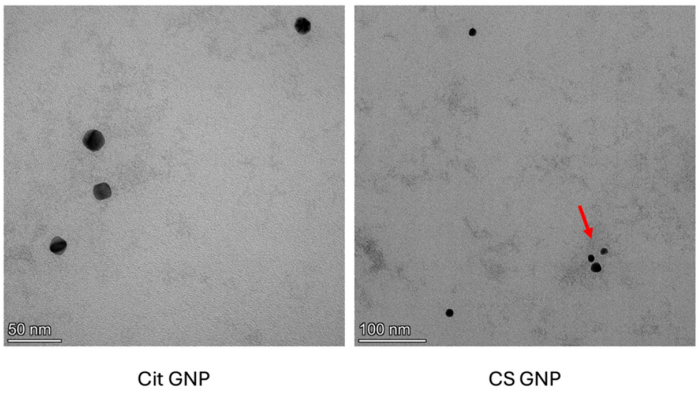


Figure 8. HRTEM images of Cit-GNPs and CS-GNPs. Red arrow indicates entrapped gold nanoparticles.

3.4.4. Fourier-Transform Infrared Spectroscopy

The formation of chitosan-capped GNPs was confirmed using FTIR spectroscopy. The FTIR spectra of pure CS and CS-coated GNPs are shown in Figure 9. In the FTIR spectrum of pure CS (Figure 9A), a prominent peak can be observed at 2869.16 cm^{-1}, corresponding to C–H stretching vibrations, which indicates the aliphatic –CH groups present in the polymer backbone. The strong bands at 1150.80, 1062.39, and 1023.89 cm^{-1} are attributed to C–O–C stretching and saccharide structures, confirming the polysaccharide nature of CS. The absorption at 894.12 cm^{-1} is characteristic of β-glycosidic linkages. In contrast, the FTIR spectrum of CS-coated GNPs shows a notable disappearance of the 2869.16 cm^{-1} peak. This suggests that the C–H stretching vibrations were suppressed upon nanoparticle formation. This disappearance is likely due to variations in the symmetry of –CHn groups during the reduction and capping process, indicating the involvement of CS functional groups in the synthesis of GNPs. The appearance of bands in the region of 1635–1652 cm^{-1} corresponds to amide I vibrations (C=O stretching) and is more pronounced in Cs-GNPs than in pure CS, indicating binding between the amino groups of chitosan and the gold surface. The broad peaks observed in the range of 3300–3400 cm^{-1} are assigned to O–H and N–H stretching, common in CS, and remain evident in GNPs, suggesting the retention of a hydrophilic character post-conjugation. The disappearance of the C–H stretching peak at 2869.16 cm^{-1}, along with shifts and intensity changes in amide and hydroxyl regions, indicate that CS effectively served as a reducing and capping agent, leading to the successful formation of CS-functionalized gold nanoparticles [36].

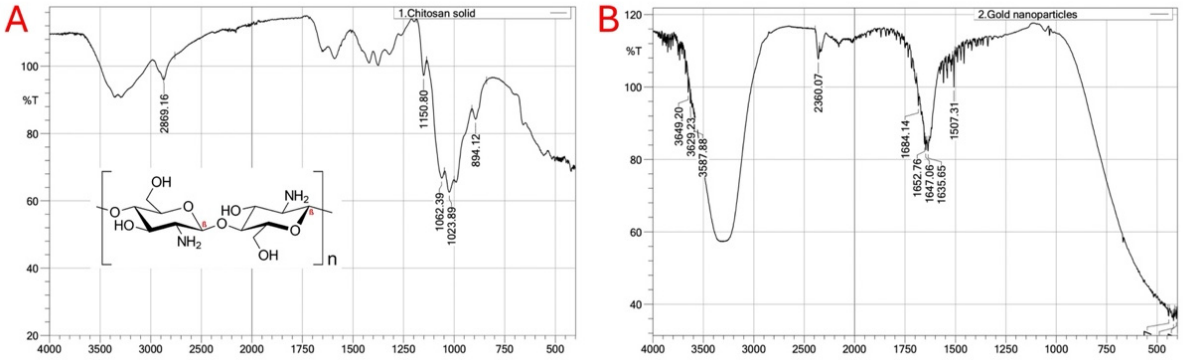


Figure 9. FTIR of pure chitosan solid (**A**) and CS-GNPs (**B**).

3.5. Gold Quantification by Inductive Coupled Plasma–Optical Emission Spectrometer

To assess the efficiency of the gold presence in our nanoparticle formulations, ICP-OES was employed for precise quantitation of the total gold content. ICP-OES exploits the characteristic emission of gold atoms—most monitored at 242.795 nm—to deliver a direct, matrix-independent measurement of the elemental gold concentration with detection limits in the low μg/mL range. Both citrate-capped (CIT-GNPs) and chitosan-coated (CS-GNPs) gold nanoparticles exhibit recoveries well above the theoretical 90 μg/mL, indicating highly efficient gold incorporation during synthesis and minimal loss during purification. CIT-GNPs exhibited a gold content of 103.09 μg/mL, corresponding to a recovery of 114.5% relative to the theoretical 90 μg/mL. CS-GNPs showed an even higher gold concentration of 115.78 μg/mL, achieving 128.6% recovery (Table 7). The elevated value for CS-GNPs likely reflects the contribution of residual gold ions adsorbed or complexed onto the chitosan coating, as well as potential enhancement of the signal due to organic matrix effects inherent to chitosan-bound gold. CS-GNPs' higher quantitation underscores the impact of surface modification on gold retention. CS's amine groups can bind residual gold species, effectively increasing the total measured gold content. This enhanced retention may improve the drug-loading capacity and stability of the nanoparticle system

but also necessitates careful consideration when translating dosing regimens from theoretical design to practical application. Overestimation of the gold concentration by ICP-OES in both nanoparticle batches may arise from several factors. First, residual unreacted gold ions adsorbed onto the chitosan coating can contribute to the measured signal, as amine groups form stable complexes. Second, matrix-induced signal enhancement may occur when organic components (e.g., citrate or chitosan residues) alter the plasma conditions, increasing the emission intensity for gold lines relative to aqueous standards. Third, incomplete blank subtraction or carry-over between samples can artificially elevate readings if acid blanks do not fully account for residual gold in the sample introduction system. Finally, polyatomic spectral interferences—such as ArCl or ArO species—may overlap with the gold emission wavelength (242.795 nm), leading to positive bias if not properly corrected by background subtraction routines [37].

Table 7. Gold content.

Sample	Gold Content (µg/mL) Theoretically	Gold Content (µg/mL) Practically with ICP-OES	Recovery (%)
Cit-GNP	90	103.09 ± 0.20	114.5
CS-GNP	90	115.78 ± 0.56	128.6

3.6. Biocompatibility of Gold Nanoparticles

The biocompatibility of GNPs is essential, since it ensure their safety and efficacy for biomedical and sensing application. Despite GNPs being generally considered among the least toxic metal NPs, their biological effects can vary significantly depending on their physicochemical properties such as size, shape, surface charge, and aggregation state, as well as the mode of administration and target tissue. Biocompatibility assessment goes beyond cytotoxicity testing, as it evaluates the absence of harmful immune responses and other adverse effects such as oxidative stress, DNA damage, or apoptosis upon interaction with biological systems. This testing is crucial to confirm that GNPs do not induce toxic or inflammatory reactions when administered, thereby enabling their safe use in drug delivery, diagnostic, and therapeutic applications. Moreover, biocompatibility testing helps us to understand the biodistribution and clearance of GNPs in the body, ensuring their efficacy without long-term toxicity. Standardized and reliable safety evaluations are required to support regulatory approval and clinical translation of GNP-based nanomedicine. The results demonstrated that cytotoxicity tested at varying concentrations of Cit-GNPs and CS-GNPs had dose-dependent viability against HaCaT and CaCO-2 cells, whereas CS showed 100% viability at the tested higher dose of 100 µg/mL (Figure 10). This result suggests that process-optimized Cit-GNPs and CS-GNPs can be used as biomedicine at lower doses. Similar results have been reported for GNPs fabricated using various reducing polymeric materials, as presented in Table 8, demonstrating the multifaceted application of metallic NPs.

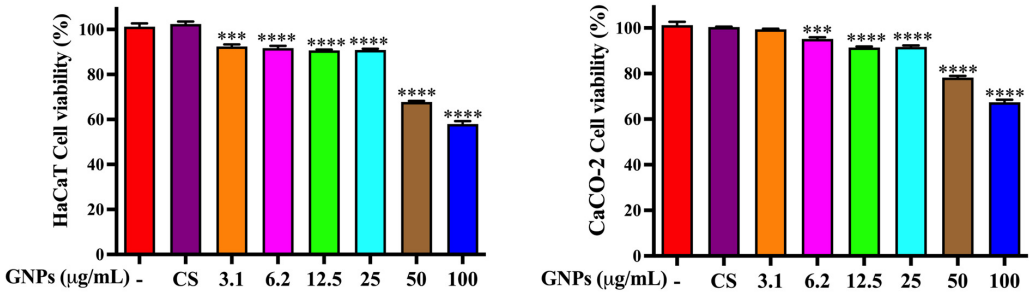


Figure 10. Biocompatibility of native chitosan and GNPs. Data displayed as mean SEM of two independent tests executed in triplicate. *** $p < 0.001$, and **** $p < 0.0001$ vs. control.

Table 8. Biocompatibility of gold nanoparticles.

Cell Line Tested	Polymeric Material Used in Fabrication of GNPs	Viability of >75% or IC_{50} at Tested Concentration of GNPs (µg/mL)	Reference
CaCo-2 and RAW 264.7	Sodium alginate	>75% at 25 µg/mL	[38]
MCF-7, MDA-MB-234, HEK-293, L-929 cells	Locust bean gum	IC_{50} at 16.17 µg/mL/25.06 µg/mL/100 µg/mL/100 µg/mL	[39]
L-929 cells	Tara gum	>95% at 100 µg/mL	[40]
HaCaT and CaCO-2 cells	Chitosan	>90% at 25 µg/mL	Present study

4. Discussion

4.1. Effect of Reducing Agent

This study contrasted chitosan and trisodium citrate as reductants. ANOVA for particle size showed a significant main effect of the reducing agent type ($p = 0.0284$), with CS generally yielding smaller particles under analogous conditions. CS acts both as a reductant and stabilizer via its amino and hydroxyl functionalities [23], often producing spherical, monodisperse GNPs in the 20–120 nm range and even below 10 nm at high CS: Au ratios. Its dual role in use yields strong electrostatic and steric stabilization, curbing aggregation [41]. CS, a deacetylated polysaccharide derived from chitin, functions dually as a green reducing agent—its electron-rich amino groups donate electrons to reduce Au^{3+} to Au^{0}—and as an electrostatic stabilizer, where protonated $–NH_3^+$ groups adsorb onto nascent AuNP surfaces, impart a high positive zeta potential, and prevent aggregation through repulsive forces, yielding monodisperse colloids whose size can be tuned by varying the chitosan concentration and reaction conditions. In acidic acetic acid media (pH ≈ 3.5–5), chitosan-capped AuNPs exhibit strong capping, demonstrated by FTIR shifts corresponding to glucosamine–gold interactions, with typical particle sizes and polydispersity indices below 0.3, depending on the polymer grade and thermal treatment [23,42]. In aqueous acidic medium, CS exhibits a polycationic nature due to the protonation of amine groups in each glucosamine repeating unit. The reduction mechanism involves three key steps: first, electrostatic attraction between protonated NH_2^+ groups and $AuCl_4^-$ ions; second, oxidation of -CHO groups at the C1 position and $-CH_2OH$ groups at the C6 position with simultaneous reduction of Au^{3+} ions; and third, Coulombic and covalent interactions causing the absorption of gold hydroxychlorides. The molecular weight of CS significantly affects the particle size, with higher-molecular-weight CS producing larger nanoparticles compared to medium-molecular-weight variants [43].

Trisodium citrate follows the classical Turkevich mechanism, where citrate ions function as both reducing and capping agents [44]. The reduction occurs through a multi-step process: initial oxidation of citrate yielding dicarboxy acetone, followed by reduction of Au^{3+} to Au^{1+}, and finally, disproportionation of aurous species to gold atoms [45]. Simultaneously, citrate ions adsorb onto nanoparticle surfaces via carboxylate ligands, imparting a negative surface charge and steric hindrance, which stabilize the colloid and control growth kinetics [46]. The citrate reduction typically produces smaller, more uniform nanoparticles (4–52 nm) with a narrow size distribution and characteristic surface plasmon resonance around 520 nm [47]. The citrate method shows superior control over the particle size through precise manipulation of citrate-to-gold ratios, with smaller particles obtained at higher citrate concentrations. It typically yields 10–25 nm GNPs at the optimal pH (~5), but larger and more polydisperse particles appear when citrate's reducing capacity or stabilizing charge is insufficient. Thus, CS's dual-function chemistry underlies its stronger

size reduction effect relative to citrate [48]. Both chitosan and trisodium citrate serve as bifunctional agents, combining reduction and stabilization to enable facile, ecofriendly synthesis of gold nanoparticles with tunable physicochemical properties.

4.2. Effect of Concentration of Reducing Agent

The concentration of the reducing agent critically determines nucleation kinetics, the growth rate, and final particle characteristics. Higher concentrations of reducing agents generally accelerate the nucleation rate, leading to smaller particles due to the rapid consumption of gold precursor before significant growth can occur [49]. In our design, the concentration of the reducing agent had a non-significant main effect on the size ($p = 0.3950$) but was significant for the PDI ($p = 0.0220$). The negative coefficient for the concentration on the PDI (–0.097) indicates that higher reductant concentrations tend to narrow size distributions. For CS-mediated green synthesis, higher CS ($\geq$0.1% w/v) produces stable, uniform round particles, whereas a lower concentration yields non-spherical or aggregated morphologies [41]. For CS, concentration effects are more complex due to its dual role as a reducer and a stabilizer. Concentrations from 0.2% to 2% show varying effects, with optimal synthesis typically occurring around 0.2–0.5% w/v [42]. Higher CS concentrations (above 1.5%) can lead to gel formation and broader particle size distributions due to increased viscosity and restricted mass transfer [42]. In citrate reduction, an intermediate citrate concentration minimizes GNPs' size by balancing nucleation and growth phases. Increasing the citrate/$HAuCl_4$ ratio accelerates nucleation, leading to smaller, more uniform particles; citrate that is too low yields bimodal or broad distributions [50]. However, excessive citrate concentrations can lead to over-stabilization and incomplete reduction [49].

4.3. Effect of Temperature

Temperature profoundly influences both reaction kinetics and nanoparticle characteristics through multiple mechanisms including the nucleation rate, growth kinetics, and thermodynamic stability. Higher temperatures accelerate the reduction process, leading to faster nanoparticle formation and improved uniformity. Studies show that elevated temperatures promote more uniform nanoparticles due to enhanced mixing and faster mass transfer [51]. Temperature effects on kinetics follow Arrhenius behavior, where small increases in temperature result in exponential increases in reaction rate. At temperatures below 90 °C, the reduction rate and overall nucleation rate decrease significantly. This temperature dependence allows for precise control over particle formation kinetics [52]. Temperature directly affects the final particle size through its influence on nucleation-to-growth ratios. Higher temperatures (90–100 °C) favor rapid nucleation overgrowth, resulting in smaller, more uniform particles. Conversely, lower temperatures (60–70 °C) promote slower nucleation but sustained growth, leading to larger particles with broader size distributions [52]. Temperature did not significantly influence the particle size ($p = 0.7044$) or the PDI ($p = 0.2230$) in the design. Higher temperatures accelerate citrate oxidation and nucleation rates, often yielding smaller, more monodisperse particles up to ~90 °C. Room-temperature citrate methods can still produce GNPs at the optimized pH, though slower growth leads to broader distributions [53].

4.4. Effect of pH

pH represents one of the most critical parameters affecting gold nanoparticle synthesis, influencing both reduction kinetics and particle stability [54]. CS-based synthesis shows a different pH dependence due to its unique reduction mechanism. An acidic pH (3.5–4.5) is essential for CS protonation and subsequent electrostatic interaction with $AuCl_4^-$ ions. At these pH values, CS exhibits the maximum reducing activity due to the optimal protonation of amino groups. As the pH increases toward neutral conditions, the CS reducing

activity decreases due to the deprotonation of amino groups, resulting in larger, less uniform particles. Above pH 7, CS may precipitate, making synthesis impractical [55]. For citrate-based synthesis, optimal pH ranges between 4.5 and 5.5 provide the most uniform, monodisperse nanoparticles. At pH 5, particles exhibit optimal characteristics: a highly monodisperse, spherical shape, narrow size distribution, and sharp surface plasmon resonance at 520 nm [56]. Below pH 4.5, the synthesis performance decreases significantly due to adverse effects on both citrate oxidation and citrate adsorption onto gold surfaces. Studies show a 46% reduction in synthesis yield when the pH drops from 5.3 to 4.7. At pH values below 4, synthesis may not occur at all due to insufficient citrate reactivity [45,55]. Above pH 6, particles become increasingly polydisperse with red-shifted plasmon peaks, indicating larger particle sizes and potential aggregation. The pH-dependent performance relates to the availability of carboxylate groups for gold binding and stabilization [45]. pH emerged as the most influential factor for both size (p = 0.0046) and the PDI (p = 0.0117). This finding aligns with the published literature, where pH has been identified as a critical parameter controlling gold nanoparticle nucleation and growth kinetics [57]. At lower pH values, the enhanced protonation of citrate groups reduces their reducing capacity and stabilization efficiency, leading to rapid nucleation and smaller particle formation. Conversely, at a higher pH, the increased availability of carboxylate groups promotes slower, more controlled growth, resulting in larger particles. A lower pH (3.5) yielded smaller, more monodisperse particles, whereas a high pH (8.5) induced larger sizes and broader PDIs. In citrate reduction, the pH modulates citrate ionization—at pH < 5, wide size distributions of polyhedral GNPs form; at pH > 6, nearly spherical, narrow distributions arise [56]. Optimal monodispersity occurs near pH 5. CS's protonation state at a low pH enhances its solubility and reducing power, thus favoring uniform nucleation and smaller GNPs.

4.5. Effect of Stirring Speed and Stirring Time

The stirring speed critically affects the mass transfer, mixing efficiency, and nanoparticle morphology during synthesis. Proper agitation ensures a uniform reactant distribution and prevents local concentration gradients that can lead to heterogeneous nucleation and growth [58]. Research demonstrates that moderate stirring speeds (500–800 rpm) typically provide optimal results for most gold nanoparticle synthesis methods. Studies using carbon monoxide reduction found that 500 rpm was optimal for producing the most monodisperse particles. Below 75 rpm, insufficient mixing leads to non-uniform particle formation and broader size distributions [47]. The stirring speed had no significant main effect on size (not listed) or the PDI (p = 0.9596). The stirring time was non-significant for size (interaction-only significance) and modestly non-significant for the PDI (p = 0.1247). Moderate stirring (≈400–500 rpm) ensures rapid mixing, promoting uniform nucleation and narrow size distributions. In Turkevich syntheses, increased stirring above ~750 rpm yielded negligible further improvements beyond ~500 rpm [47]. Excessive stirring can reduce local supersaturation, decrease nucleation sites, and paradoxically increase the particle size [12].

4.6. Citrate-Capped (Cit-GNP) and Chitosan-Capped (CS-GNP) Gold Nanoparticles

Gold nanoparticles were prepared using two different methods: Turkevich (Cit-GNPs) and direct reduction using CS (CS-GNPs). The LSPR peak for both Cit-GNPs and CS-GNPs observed between 520 and 530 nm wavelengths confirms the successful gold nanoparticle formation with characteristic optical properties, where the sharp and intense absorption band indicates the collective resonant oscillation of conduction band electrons. CS-GNPs demonstrated superior surface plasmon resonance properties, with a characteristic absorption peak at 522 nm and higher absorbance intensity, indicating well-formed spherical gold nanoparticles with enhanced optical stability compared to B7, which exhibited a broader

SPR peak at 528 nm with reduced intensity. The blue shift observed in the LSPR effect of B7 indicates the better reducing capabilities and stabilizing properties of CS. The hydrodynamic diameter for CS-GNPs is ~45.68 nm when using CS as the reducing agent, whereas the TSC yields GNPs with a hydrodynamic diameter of ~96.69 nm. The morphological results and difference in hydrodynamic diameter observed were due to the stern layer and slipping pane of both GNPs. Moreover, the zeta potential for CS-GNPs and Cit-GNPs suggested strong colloidal stability for both GNPs. FTIR analysis confirmed the formation of CS-GNPs, as evident from the disappearance of the C–H stretching peak at 2869.16 cm^{-1} and enhanced amide I bands (1635–1652 cm^{-1}), indicating the interaction of CS amino groups with the gold surface. The retention of broad O–H and N–H peaks (3300–3400 cm^{-1}) suggests preserved hydrophilicity. ICP-OES quantification confirmed efficient gold incorporation in both NP formulations, with recoveries exceeding the theoretical 90 μg/mL. The higher gold content in CS-GNPs likely arises from residual gold ions bound to chitosan's amine groups and possible matrix effects, highlighting the role of surface modification in enhancing gold retention, stability, and potential drug-loading capacity. These spectral shifts demonstrate the role of chitosan as both a reducing and capping agent in GNP synthesis. The cytotoxicity assay showed that cell viability was reduced in both Cit-GNP and CS-GNP preparations in HaCaT and CaCO-2 cells depending on the concentration of the nanoparticles, thus suggesting that the degree of cellular response was directly related to the nanoparticle concentration. Conversely, chitosan (CS) itself did not show cytotoxicity, and cell viability was almost 100%, even at the highest concentration (100 μg/mL). These observations underscore the biocompatibility of CS as a polymeric stabilizer and imply that the optimized Cit-GNP and CS-GNP preparations can be used in lower amounts without any issues of safety. Together, the findings indicate that these nanoparticle systems might be applicable to the biomedical situation, if dose factors are taken into account and cytotoxic effects are minimized. The comprehensive characterization of synthesized GNPs reveals optimal physicochemical properties suitable for numerous biomedical applications.

5. Conclusions

In this study, a 2^{6-2} fractional factorial design (FFD) was successfully employed to screen and identify the critical process parameters influencing the synthesis of gold nanoparticles (GNPs) using CS and trisodium citrate as reducing and stabilizing agents. The key objective was to understand how six independent variables—type of reducing agent, its concentration, reaction temperature, pH, stirring speed, and stirring time—affect the particle size and polydispersity index (PDI) of the synthesized GNPs. The statistical analysis revealed that pH was the most influential factor, significantly affecting both particle size and the PDI. A lower pH (3.5) favored the formation of smaller, more monodisperse nanoparticles, likely due to enhanced nucleation and faster reduction kinetics, while a higher pH (8.5) led to larger and more polydisperse particles. The type of reducing agent also played a significant role, with CS producing smaller and more uniform nanoparticles compared to trisodium citrate, attributed to its dual role in reduction and steric stabilization via its amino and hydroxyl groups. The concentration of reducing agent, though not significant for particle size, had a notable impact on the PDI, where higher concentrations resulted in narrower size distributions. Other factors such as temperature, stirring speed, and stirring time were found to have comparatively less significant individual effects, though some interactions, such as between reducing agent type, concentration, and stirring time, demonstrated a notable influence on nanoparticle uniformity. The UV-Vis spectra confirmed the presence of LSPR, with peak shifts correlating with the particle size and dispersity. Overall, the use of FFD provided a statistically robust and resource-efficient method for identifying significant formulation variables in gold nanoparticle synthesis.

The findings highlight that careful control of pH and selection of a biocompatible reducing agent like CS are crucial for producing GNPs with an optimal size and stability. Moreover, the use of green synthesis via CS supports the ongoing push toward safer, more sustainable nanomaterial development. In conclusion, the integrated approach of factorial screening, physicochemical characterization, and green chemistry demonstrates a rational strategy for the controlled synthesis of gold nanoparticles with desired attributes, underscoring the critical interplay between formulation variables and nanoparticle properties.

Author Contributions: Conceptualization, K.R. and H.J.; methodology, K.R.; software, H.J. and K.R.; validation, V.R.C., P.M. and S.S.; formal analysis, K.R.; investigation, H.J.; resources, K.R.; data curation, H.J.; writing—original draft preparation, H.J.; writing—review and editing, H.J., K.R. and S.S.; visualization, V.R.C. and P.M.; supervision, K.R.; project administration, K.R. All authors have read and agreed to the published version of the manuscript.

Funding: This research was funded by the Gujarat State Biotechnology Mission, Department of Science and Technology, Government of Gujarat, grant number: GSBTM/JD(R&D)/618/21-22/00003682.

Data Availability Statement: The data presented in this study are available on request from the corresponding author.

Acknowledgments: The authors would like to acknowledge the Gujarat State Biotechnology Mission (GSBTM/JD(R&D)/618/21-22/00003682, Department of Science and Technology, Government of Gujarat, Gujarat, India) for its financial support, and the Principal of L. M. College of Pharmacy for providing the necessary support to carry out this study.

Conflicts of Interest: The authors declare no conflicts of interest, financial or otherwise.

Abbreviations

The following abbreviations are used in this manuscript:

CS-GNP	Chitosan-capped Gold Nanoparticle
Cit-GNP	Citrate-capped Gold Nanoparticle
NP	Nanoparticle
LSPR	Local Surface Plasmon Resonance
TEM	Transmission Electron Microscopy
FFD	Fractional Factorial Design
GNP	Gold Nanoparticle

References

1. Mingos, D.M.P. (Ed.) Historical Introduction to Gold Colloids, Clusters and Nanoparticles. In *Gold Clusters, Colloids and Nanoparticles I*; Springer International Publishing: Cham, Switzerland, 2014; pp. 1–47.
2. Mayoral, Á.; Agúndez, J.; Pascual-Valderrama, I.M.; Pérez-Pariente, J. Generation of gold nanoparticles according to procedures described in the eighteenth century. *Gold Bull.* **2014**, *47*, 161–165. [CrossRef]
3. Jennings, T.; Strouse, G. Past, Present, and Future of Gold Nanoparticles. In *Bio-Applications of Nanoparticles*; Chan, W.C.W., Ed.; Springer: New York, NY, USA, 2007; pp. 34–47.
4. Dykman, L.; Khlebtsov, B.; Khlebtsov, N. Drug delivery using gold nanoparticles. *Adv. Drug Deliv. Rev.* **2025**, *216*, 115481. [CrossRef]
5. Ranch, K.; Jani, H.; Patel, Y.; Patel, C.; Babu, R.J.; Tiwari, A.K.; Bhandare, R.R.; Boddu, S.H.S. Chapter 12—Gold nanoparticles in colon targeting. In *Nanocarriers Based Colon Targeting*; Kumar, L., Pathak, Y.V., Eds.; Academic Press: New York, NY, USA, 2025; pp. 285–312.
6. Liu, J.; Wang, X.; Yuan, L.; Zhao, Y.; Zhang, Y.; Wu, Y.; Liu, M. Hairpin DNA-functionalized gold nanoparticles for diagnostic imaging and overcoming doxorubicin resistance: Enhanced drug loading and cytotoxicity based on thermodynamic guidance. *J. Mol. Struct.* **2025**, *1337*, 142264. [CrossRef]
7. Moreira, A.F.; Filipe, H.A.L.; Miguel, S.P.; Ribeiro, M.J.; Coutinho, P. Recent advances in smart gold nanoparticles for photothermal therapy. *Nanomedicine* **2025**, *20*, 1339–1353. [CrossRef] [PubMed]

8. Panagopoulos, D.; Alamdari, A.A.; Quinson, J. Surfactant-free colloidal gold nanoparticles: Room temperature synthesis, size control and opportunities for catalysis. *Mater. Today Nano* **2025**, *29*, 100600. [CrossRef]
9. El-Deen, A.K.; Hussain, C.M. Bio-based gold nanoparticles for environmental and forensic samples: State of the art with a sustainable way forward. *TrAC Trends Anal. Chem.* **2025**, *183*, 118113. [CrossRef]
10. Zhang, P.; Hou, H.; Xu, S.; Wen, Y.; Zhang, Y.; Xing, F. Localized surface plasmon resonance sensing based on monometallic gold nanoparticles: From material preparation to detection of bioanalytes. *Anal. Methods* **2025**, *17*, 892–915. [CrossRef]
11. Kimling, J.; Maier, M.; Okenve, B.; Kotaidis, V.; Ballot, H.; Plech, A. Turkevich Method for Gold Nanoparticle Synthesis Revisited. *J. Phys. Chem. B* **2006**, *110*, 15700–15707. [CrossRef]
12. Dong, J.; Carpinone, P.L.; Pyrgiotakis, G.; Demokritou, P.; Moudgil, B.M. Synthesis of Precision Gold Nanoparticles Using Turkevich Method. *Kona* **2020**, *37*, 224–232. [CrossRef]
13. Perala, S.R.K.; Kumar, S. On the Mechanism of Metal Nanoparticle Synthesis in the Brust–Schiffrin Method. *Langmuir* **2013**, *29*, 9863–9873. [CrossRef]
14. Kirichkov, M.V.; Guda, A.A.; Budnyk, A.P.; Lastovina, T.A.; Bugaev, A.L.; Shapovalov, V.V.; Rusalev, Y.V.; Chernyshev, A.V.; Soldatov, A.V. In situ analysis of the formation steps of gold nanoparticles by oleylamine reduction. *J. Struct. Chem.* **2017**, *58*, 1403–1410. [CrossRef]
15. National Institutes of Health (NIH). *Sodium Borohydride | NaBH4 | CID 4311764*; PubChem: Bethesda, MD, USA, 2005.
16. Alkilany, A.M.; Murphy, C.J. Toxicity and cellular uptake of gold nanoparticles: What we have learned so far? *J. Nanopart. Res.* **2010**, *12*, 2313–2333. [CrossRef]
17. Pang, F.; Cheng, S.; Yang, H.; Hu, W. Oleylamine-Functionalized Graphene Oxide in Wearable Flexible Organic Field-Effect Transistors for Ultrasensitive NH3 Detection. *ACS Sens.* **2025**, *10*, 4318–4328. [CrossRef] [PubMed]
18. Abdelhamid, H.N.; El-Bery, H.M.; Metwally, A.A.; Elshazly, M.; Hathout, R.M. Synthesis of CdS-modified chitosan quantum dots for the drug delivery of Sesamol. *Carbohydr. Polym.* **2019**, *214*, 90–99. [CrossRef] [PubMed]
19. Panda, P.K.; Sadeghi, K.; Seo, J. Recent advances in poly (vinyl alcohol)/natural polymer based films for food packaging applications: A review. *Food Packag. Shelf Life* **2022**, *33*, 100904. [CrossRef]
20. Panda, P.K.; Yang, J.-M.; Chang, Y.-H.; Su, W.-W. Modification of different molecular weights of chitosan by p-Coumaric acid: Preparation, characterization and effect of molecular weight on its water solubility and antioxidant property. *Int. J. Biol. Macromol.* **2019**, *136*, 661–667. [CrossRef]
21. Fernández-Pan, I.; Maté, J.I.; Gardrat, C.; Coma, V. Effect of chitosan molecular weight on the antimicrobial activity and release rate of carvacrol-enriched films. *Food Hydrocoll.* **2015**, *51*, 60–68. [CrossRef]
22. Fuster, M.G.; Montalbán, M.G.; Carissimi, G.; Lima, B.; Feresin, G.E.; Cano, M.; Giner-Casares, J.J.; López-Cascales, J.J.; Enriz, R.D.; Víllora, G. Antibacterial Effect of Chitosan–Gold Nanoparticles and Computational Modeling of the Interaction between Chitosan and a Lipid Bilayer Model. *Nanomaterials* **2020**, *10*, 2340. [CrossRef]
23. Hashem, A.H.; Shehabeldine, A.M.; Ali, O.M.; Salem, S.S. Synthesis of Chitosan-Based Gold Nanoparticles: Antimicrobial and Wound-Healing Activities. *Polymers* **2022**, *14*, 2293. [CrossRef]
24. Corbierre, M.K.; Cameron, N.S.; Lennox, R.B. Polymer-Stabilized Gold Nanoparticles with High Grafting Densities. *Langmuir* **2004**, *20*, 2867–2873. [CrossRef]
25. Delong, R.K.; Reynolds, C.M.; Malcolm, Y.; Schaeffer, A.; Severs, T.; Wanekaya, A. Functionalized gold nanoparticles for the binding, stabilization, and delivery of therapeutic DNA, RNA, and other biological macromolecules. *Nanotechnol. Sci. Appl.* **2010**, *3*, 53–63. [CrossRef]
26. Chompoosor, A.; Han, G.; Rotello, V.M. Charge Dependence of Ligand Release and Monolayer Stability of Gold Nanoparticles by Biogenic Thiols. *Bioconjugate Chem.* **2008**, *19*, 1342–1345. [CrossRef]
27. Politis, S.N.; Colombo, P.; Colombo, G.; Rekkas, D.M. Design of experiments (DoE) in pharmaceutical development. *Drug Dev. Ind. Pharm.* **2017**, *43*, 889–901. [CrossRef] [PubMed]
28. Fukuda, I.; Pinto, C.; Moreira, C.; Saviano, A.; Lourenço, F. Design of Experiments (DoE) applied to Pharmaceutical and Analytical Quality by Design (QbD). *Braz. J. Pharm. Sci.* **2018**, *54*, e01006. [CrossRef]
29. 5.3.3.2. Randomized Block Designs. Available online: https://www.itl.nist.gov/div898/handbook/pri/section3/pri332.htm (accessed on 20 September 2025).
30. Aizpurua, O.; Alberdi, A.; Aihartza, J.; Garin, I. Fishing Technique of Long-Fingered Bats Was Developed from a Primary Reaction to Disappearing Target Stimuli. *PLoS ONE* **2016**, *11*, 12. [CrossRef] [PubMed]
31. Jayeoye, T.J.; Singh, S.; Eze, F.N.; Olatunji, O.J.; Olatunde, O.O.; Omaka, O.N.; Odogiyon, O.B.; Okpara, K.E. Exploration of Biocompatible Ascorbic Acid Reduced and Stabilized Gold Nanoparticles, as Sensitive and Selective Detection Nanoplatform for Silver Ion in Solution. *Plasmonics* **2025**, *20*, 1841–1858. [CrossRef]
32. Maulvi, F.A.; Patel, A.R.; Shetty, K.H.; Desai, D.T.; Shah, D.O.; Willcox, M.D.P. Chitosan nanoparticles laden contact lenses for enzyme-triggered controlled delivery of timolol maleate: A promising strategy for managing glaucoma. *Drug Deliv. Transl. Res.* **2024**, *14*, 3212–3224. [CrossRef]

33. Jayeoye, T.J.; Panghiyangani, R.; Singh, S.; Muangsin, N. Quercetin Reduced and Stabilized Gold Nanoparticle/Al^{3+}: A Rapid, Sensitive Optical Detection Nanoplatform for Fluoride Ion. *Nanomaterials* **2024**, *14*, 1967. [CrossRef]
34. Teeling, E.C.; Springer, M.S.; Madsen, O.; Bates, P.; O'Brien, S.J.; Murphy, W.J. A molecular phylogeny for bats illuminates biogeography and the fossil record. *Science* **2005**, *307*, 580–584. [CrossRef]
35. Lanza, G.; Betancourth, D.; Avila, A.; Riascos, H.; Perez-Taborda, J.A. Control of the size distribution of AuNPs for colorimetric sensing by pulsed laser ablation in liquids. *Kuwait J. Sci.* **2025**, *52*, 100294. [CrossRef]
36. Silva, A.; Coelho, A.; Lopes, L.; Martins, M.; Crespilho, F.; Merkoçi, A.; Cantanhêde, W. Nano-Assembled Supramolecular Films from Chitosan-Stabilized Gold Nanoparticles and Cobalt(II) Phthalocyanine. *J. Braz. Chem. Soc.* **2013**, *24*, 1237–1245. [CrossRef]
37. DeSousa, J.M.; Jorge, M.Z.; Lindsay, H.B.; Haselton, F.R.; Wright, D.W.; Scherr, T.F. Inductively coupled plasma optical emission spectroscopy as a tool for evaluating lateral flow assays. *Anal. Methods* **2021**, *13*, 2137–2146. [CrossRef]
38. Jayeoye, T.J.; Eze, F.N.; Singh, S.; Olatunde, O.O.; Benjakul, S.; Rujiralai, T. Synthesis of gold nanoparticles/polyaniline boronic acid/sodium alginate aqueous nanocomposite based on chemical oxidative polymerization for biological applications. *Int. J. Biol. Macromol.* **2021**, *179*, 196–205. [CrossRef] [PubMed]
39. Eze, F.N.; Eze, R.C.; Okpara, K.E.; Adekoya, A.E.; Kalu, H.N. Design and development of locust bean gum-endowed/Phyllanthus reticulatus anthocyanin- functionalized biogenic gold nanosystem for enhanced antioxidative and anticancer chemotherapy. *Int. J. Biol. Macromol.* **2024**, *275*, 133687. [CrossRef] [PubMed]
40. Eze, F.N.; Eze, R.C.; Ovatlarnporn, C. Insights into the remarkable attenuation of hen egg white lysozyme amyloid fibril formation mediated by biogenic gold nanoparticles stabilized by quercetin-functionalized tara gum. *Int. J. Biol. Macromol.* **2023**, *232*, 123044. [CrossRef] [PubMed]
41. Sun, L.; Li, J.; Cai, J.; Zhong, L.; Ren, G.; Ma, Q. One pot synthesis of gold nanoparticles using chitosan with varying degree of deacetylation and molecular weight. *Carbohydr. Polym.* **2017**, *178*, 105–114. [CrossRef]
42. Mohan, C.O.; Gunasekaran, S.; Ravishankar, C.N. Chitosan-capped gold nanoparticles for indicating temperature abuse in frozen stored products. *Npj Sci. Food* **2019**, *3*, 2. [CrossRef]
43. Sreelakshmi, K.R.; Mohan, C.O.; Remya, S.; Raj, R.; Rajasree, R.; Pillai, D.; Kumar, K.A.; Ravishankar, C.N. Time dependent synthesis of gold nanoparticles using chitosan as reducing agent: A spectroscopic approach. *Indian J. Fish.* **2021**, *68*, 112–117. [CrossRef]
44. Li, C.; Li, D.; Wan, G.; Xu, J.; Hou, W. Facile synthesis of concentrated gold nanoparticles with low size-distribution in water: Temperature and pH controls. *Nanoscale Res. Lett.* **2011**, *6*, 440. [CrossRef]
45. Contreras-Trigo, B.; Díaz-García, V.; Guzmán-Gutierrez, E.; Sanhueza, I.; Coelho, P.; Godoy, S.E.; Torres, S.; Oyarzún, P. Slight pH Fluctuations in the Gold Nanoparticle Synthesis Process Influence the Performance of the Citrate Reduction Method. *Sensors* **2018**, *18*, 2246. [CrossRef]
46. Dinh, T.; Dobó, Z.; Palotás, Á.B.; Kovács, H. A review of gold nanoparticle synthesis: Transitioning from conventional techniques to plant-mediated green nanofabrication. *Mater. Today Chem.* **2025**, *48*, 103003. [CrossRef]
47. Young, J.K.; Lewinski, N.A.; Langsner, R.J.; Kennedy, L.C.; Satyanarayan, A.; Nammalvar, V.; Lin, A.Y.; Drezek, R.A. Size-controlled synthesis of monodispersed gold nanoparticles via carbon monoxide gas reduction. *Nanoscale Res. Lett.* **2011**, *6*, 428. [CrossRef] [PubMed]
48. Patungwasa, W.; Hodak, J.H. pH tunable morphology of the gold nanoparticles produced by citrate reduction. *Mater. Chem. Phys.* **2008**, *108*, 45–54. [CrossRef]
49. Aljarrah, M.T.; Alboull, A.a.M.; Alharahsheh, M.S.; Ashraf, A.; Khandakar, A. Parametric Study of Gold Nanoparticles Synthesis under Micro-Continuous Flow Conditions. *Molecules* **2022**, *27*, 8651. [CrossRef]
50. Kim, H.-s.; Seo, Y.S.; Kim, K.; Han, J.W.; Park, Y.; Cho, S. Concentration Effect of Reducing Agents on Green Synthesis of Gold Nanoparticles: Size, Morphology, and Growth Mechanism. *Nanoscale Res. Lett.* **2016**, *11*, 230. [CrossRef]
51. Mountrichas, G.; Pispas, S.; Kamitsos, E.I. Effect of Temperature on the Direct Synthesis of Gold Nanoparticles Mediated by Poly(dimethylaminoethyl methacrylate) Homopolymer. *J. Phys. Chem. C* **2014**, *118*, 22754–22759. [CrossRef]
52. Manta, P.; Chandra Singh, S.; Deep, A.; Kapoor, D.N. Temperature-regulated gold nanoparticle sensors for immune chromatographic rapid test kits with reproducible sensitivity: A study. *IET Nanobiotechnol.* **2021**, *15*, 338–346. [CrossRef]
53. Oliveira, A.E.F.; Pereira, A.C.; Resende, M.A.C.; Ferreira, L.F. Gold Nanoparticles: A Didactic Step-by-Step of the Synthesis Using the Turkevich Method, Mechanisms, and Characterizations. *Analytica* **2023**, *4*, 250–263. [CrossRef]
54. Sun, L.; Zhang, Z.; Wang, S.; Zhang, J.; Li, H.; Ren, L.; Weng, J.; Zhang, Q. Effect of pH on the Interaction of Gold Nanoparticles with DNA and Application in the Detection of Human p53 Gene Mutation. *Nanoscale Res. Lett.* **2008**, *4*, 216. [CrossRef]
55. Ariski, R.T.; Lee, K.K.; Kim, Y.; Lee, C.-S. The impact of pH and temperature on the green gold nanoparticles preparation using Jeju Hallabong peel extract for biomedical applications. *RSC Adv.* **2024**, *14*, 14582–14592. [CrossRef]
56. Tyagi, H.; Kushwaha, A.; Kumar, A.; Aslam, M. A Facile pH Controlled Citrate-Based Reduction Method for Gold Nanoparticle Synthesis at Room Temperature. *Nanoscale Res. Lett.* **2016**, *11*, 362. [CrossRef]

57. Yazdani, S.; Daneshkhah, A.; Diwate, A.; Patel, H.; Smith, J.; Reul, O.; Cheng, R.; Izadian, A.; Hajrasouliha, A.R. Model for Gold Nanoparticle Synthesis: Effect of pH and Reaction Time. *ACS Omega* **2021**, *6*, 16847–16853. [CrossRef]
58. García, M.A.; Bouzas, V.; Carmona, N. Influence of stirring in the synthesis of gold nanorods. *Mater. Chem. Phys.* **2011**, *127*, 446–450. [CrossRef]

Disclaimer/Publisher's Note: The statements, opinions and data contained in all publications are solely those of the individual author(s) and contributor(s) and not of MDPI and/or the editor(s). MDPI and/or the editor(s) disclaim responsibility for any injury to people or property resulting from any ideas, methods, instructions or products referred to in the content.